Supporting Information

Interference of Phosphate in Adsorption of Arsenate and Arsenite over Confined Metastable Two-Line Ferrihydrite and Magnetite

Chennu Sudhakar,[†] Sritama Mukherjee,[†] Avula Anil Kumar,[†] Ganesan Paramasivam,[†] P. Karthigai Meena,[†] Nonappa,[‡] and Thalappil Pradeep[,†]*

[†] DST Unit of Nanoscience (DST UNS) and Thematic Unit of Excellence (TUE), Department of Chemistry, Indian Institute of Technology Madras, Chennai 600036, India.

[‡]Faculty of Engineering and Natural Sciences, Tampere University, FI-33101, Tampere, Finland.

* Corresponding author

Thalappil Pradeep: pradeep@iitm.ac.in

Thalappil Pradeep, DST Unit of Nanoscience (DST UNS) and Thematic Unit of Excellence (TUE), Department of Chemistry, Indian Institute of Technology Madras, Chennai 600036, India.

Tel.: +91-44 2257 4208; Fax: +91-44 2257 0545/0509

SUPPORTING INFORMATION CONTENT

Total number of pages: 20

Total number of figures: 8

Total number of tables: 3

TABLE OF CONTENTS

MATERIALS

Potassium dihydrogen ortho phosphate (KH_2PO_4), Sodium arsenite ($NaAsO_2$), and disodium hydrogen arsenate ($Na_2HAsO_4 \cdot 7H_2O$) were purchased from SD Fine Chemicals Limited. Magnetite (Fe_3O_4) was purchased from Alfa Aesar. The syntheis of confined metastable 2-line

ferrihydrite (CM2LF) was reported earlier.[1] Sodium hydroxide (NaOH) was purchased from Rankem Glasswares and Chemicals Pvt. Ltd., India. Hydrochloric acid (HCl) was purchased from Merck Life Science Pvt. Ltd., India. All chemicals were of analytical grade and were used without further purification. Deionized (DI) water was used throughout the experiments.

INSTRUMENTATION

X-ray Photoelectron Spectroscopy (XPS): measurements were done using an ESCA Probe TPD spectrometer of Omicron Nanotechnology. Polychromatic Al Kα was used as the X-ray source (hν = 1486.6 eV). Binding energy was calibrated with respect to C 1s at 284.8 eV. All the XPS spectra were deconvoluted using Casa XPS software. A PerkinElmer FTIR spectrometer was used to measure the infrared spectra. The spectrometer resolution was kept at 4 cm^{-1}. All the IR spectra were deconvoluted using Origin Pro 9.0 software. Various model building software were used to build the structures. The rectangular slab was built by using VESTA and Avogadro 1.2.0 software.

Transmission Electron Microscopy (TEM): TEM images were collected using JEM 3200FSC field emission microscope (JEOL) operated at 300 kV in bright field mode with Omega-type Zero-loss energy filter. The images were acquired with GATAN DIGITAL MICROGRAPH software while the specimen temperature was maintained at -187 ºC.

Sample Preparation: The TEM samples were prepared by placing 5 µL aqueous dispersion (~5 mg/ mL) 300 hexagonal mesh Ni grid with ultrathin carbon support film. The grids were plasma cleaned for 30 s before use. After placing the aqueous dispersion, the grids were subjected to cleaning by dipping them in double-distilled water for 2 x15 s. The specimen was then dried under ambient conditions for 24 h before imaging.

SerialEM and Electron Tomographic Reconstruction: The tilt series were acquired with the SerialEM-software package.[2] Samples were tilted between ±69º angles with 3º increment steps.[3] Prealignment of tilt image series was, and the fine alignment and cropping were executed with IMOD.[4] The images were binned twice to reduce noise and computation time. Maximum entropy method (MEM) reconstruction scheme was carried out with a custom-made program on Mac or Linux cluster with a regularization parameter value of λ=1.0e^3.[4-5]

THEORETICAL CALCULATIONS

To find binding energy (BE) of P 2p in various phosphorous complexes used equation is $T_{BE2} = -E + R = \Delta$ [Tardio *et al.*, 2018], E equals to orbital energy of ejected electron from its orbit according to Koopman theorem ($-E = T_{BE1} = K$) and R is orbital relaxation after ionization. The electron correlation function is needed to add to the given equation ($T_{BE3} = -E + R + \Delta C$) to get more accurate results. Two calculations are needed to find the binding energy of a particular atom in a molecule using ΔSCF method. The first calculation involves optimizing the geometry of the molecule(or ion) and the chance to spot and find the locations of the orbitals of concern. The second calculation (which involves finding the energy of the core ionized molecule) requires two steps while executed with GAUSSIAN 09. The first step requires the interchange of the core orbital of interest with the highest occupied molecular orbital (HOMO). The second step involves ionization of a given molecule or ion that means an electron will be taken from the exchanged core orbital (2p) which is switched from core level to HOMO. The steps followed for binding energy calculation of the core electron are explained in detail in Tardio *et al.*, 2018.

DFT CALCULATIONS ON POSSIBLE PHOSPHATE COMPLEXES WITH $Fe_2O_{10}H_Y$

To support the XPS results, as a first step, DFT calculations were performed on two phosphate species, which exist in natural waters at pH 7. To determine the P 2p binding energy of $H_2PO_4^{1-}$ / HPO_4^{2-}species theoretically, two methods were used such as Hartree Fock (HF) and B3LYP (Becke, 3-parameter, Lee–Yang–Parr) method with (or without) solvent effect. The B3LYP method with solvent effect gave the best results for $H_2PO_4^{1-}$/ HPO_4^{2-} among other methods, using a basis set of 6-31G. These results are shown in Table S2. Therefore, the B3LYP method was chosen to find the T_{BE} of P 2p in various complexes. Finally, the B3LYP method was chosen without including the solvent effect for additional calculations in order to reduce the computational cost. Further theoretical calculations of binding energy have been extended to As(III/V) complexes.

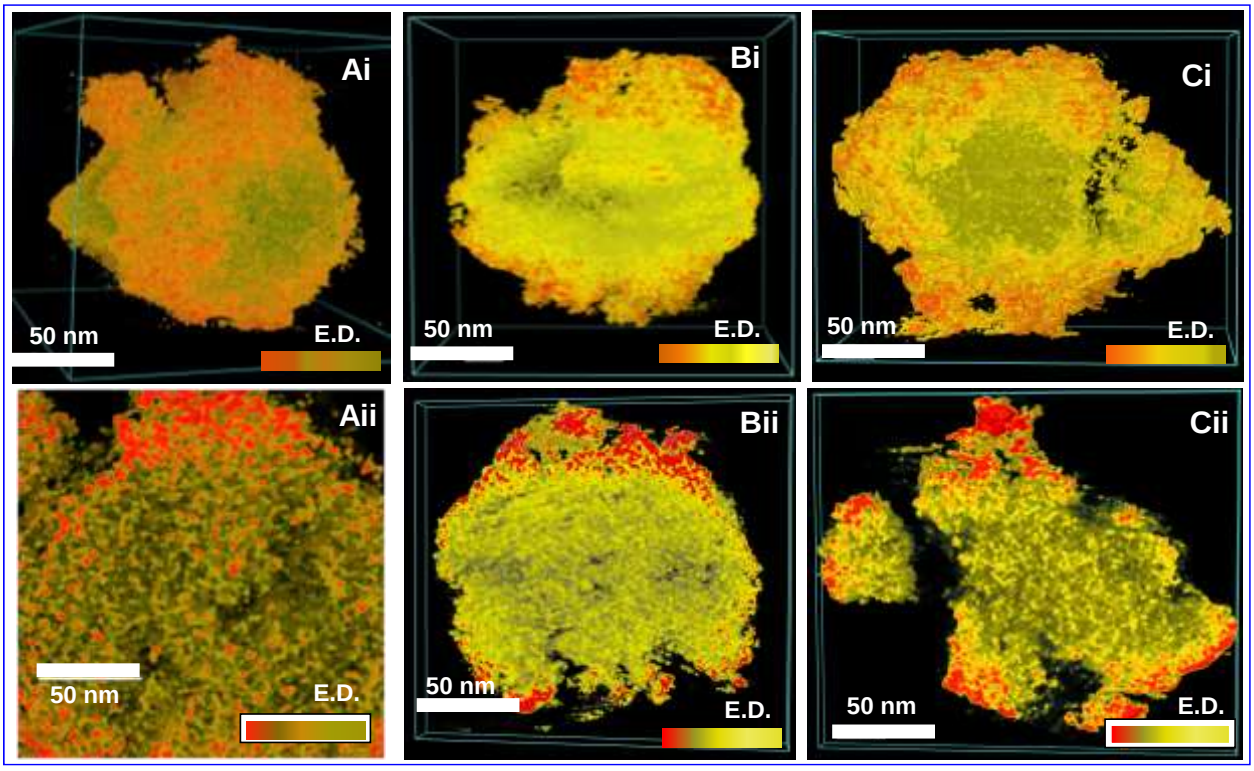

Figure S1. 3D reconstructed images of 2-line ferrihydrite composite (CM2LF) before and after arsenic treatment. Ai and Aii) CM2LF and its cross-sectional view before arsenic treatment. Bi and Bii) As (III) adsorbed CM2LF with and its cross-sectional view. Ci and Cii) As (V) adsorbed CM2LF and its cross-sectional view. E.D. refers to electron density.

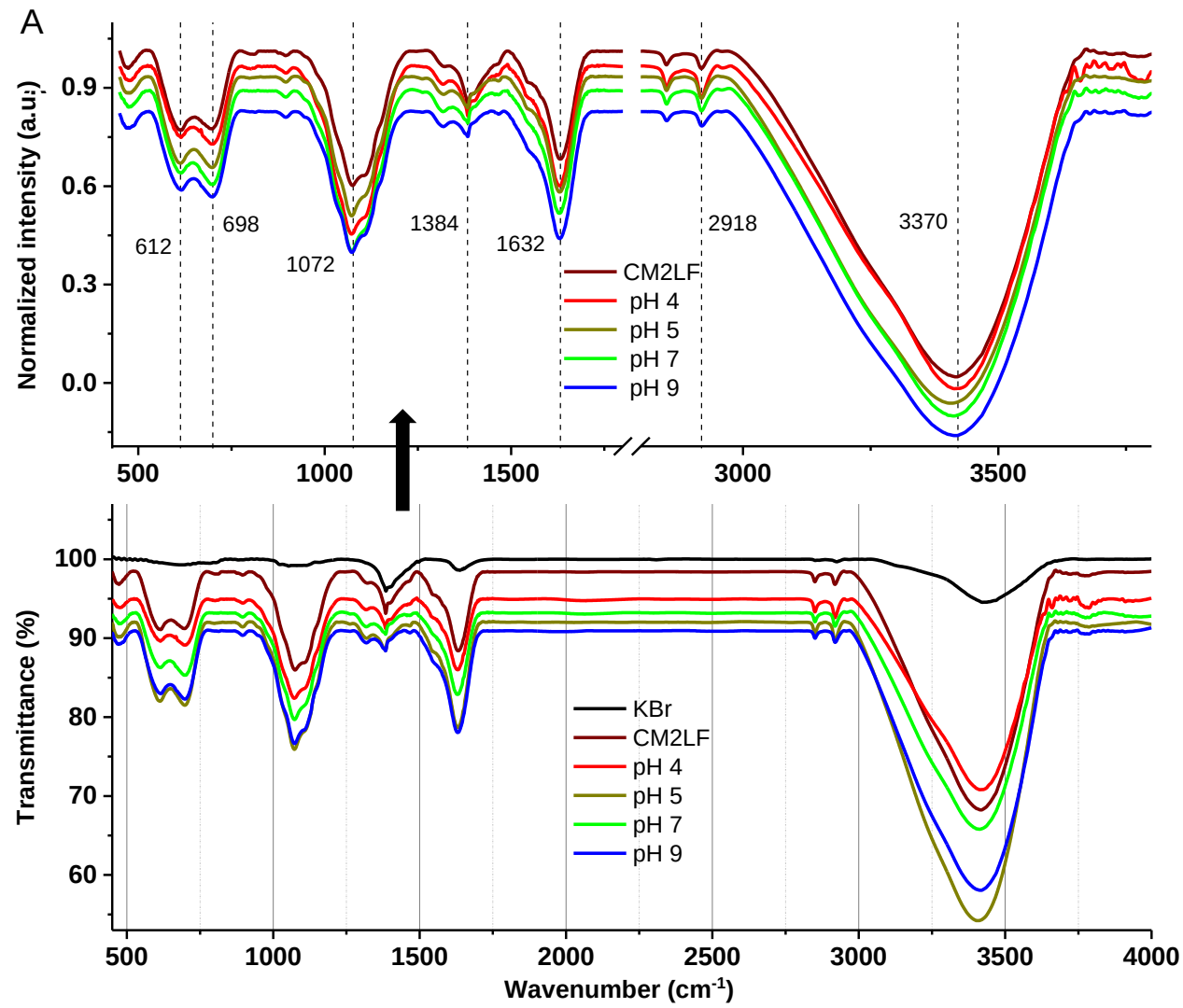
A
Normalized intensity (a.u.)
612
698
1072
1384
1632
2918
3370
CM2LF
pH 4
pH 5
pH 7
pH 9
Transmittance (%)
KBr
CM2LF
pH 4
pH 5
pH 7
pH 9
Wavenumber (cm-1)

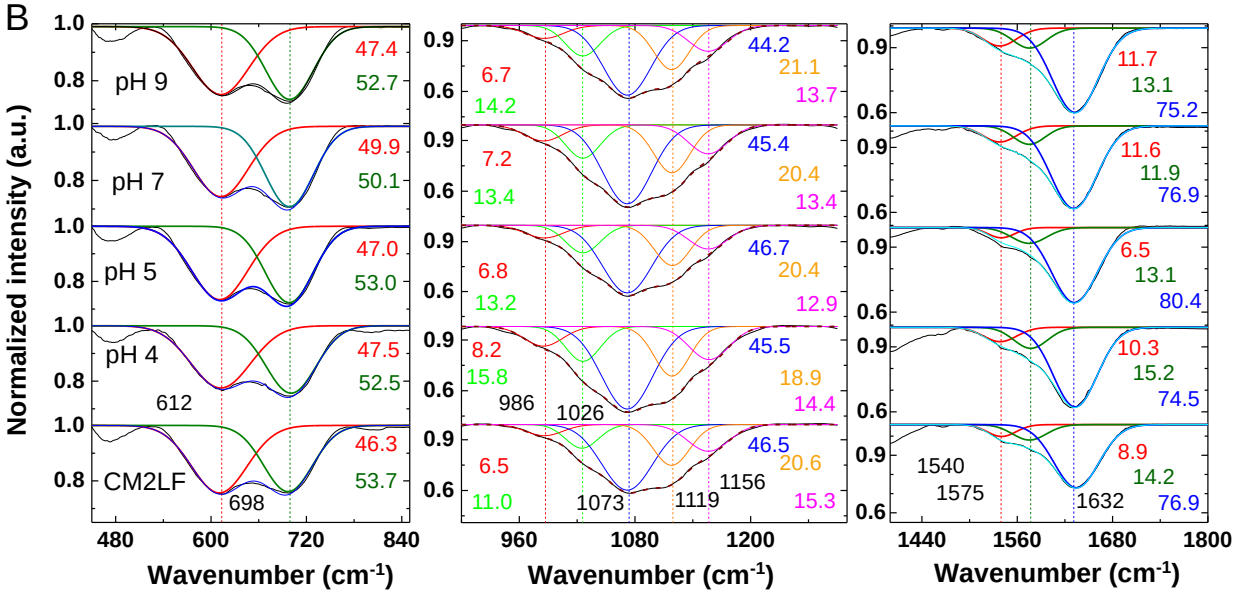
B
Normalized intensity (a.u.)
pH 9
47.4
52.7
pH 7
49.9
50.1
pH 5
47.0
53.0
pH 4
47.5
52.5
612
CM2LF
46.3
53.7
698
6.7
14.2
44.2
21.1
13.7
7.2
13.4
45.4
20.4
13.4
6.8
13.2
46.7
20.4
12.9
8.2
15.8
986
1026
45.5
18.9
14.4
6.5
11.0
1073
1119
1156
46.5
20.6
15.3
11.7
13.1
75.2
11.6
11.9
76.9
6.5
13.1
80.4
10.3
15.2
74.5
1540
1575
1632
8.9
14.2
76.9
Wavenumber (cm-1)
Wavenumber (cm-1)
Wavenumber (cm-1)

Figure S2. (A) FTIR spectra of CM2LF and CM2LF in distilled water at various pH: 4, 5, 7, and 9, also included only KBr. (B) zoomed spectra of (A) in three different regions 450 to 850, 900 to1300, and 1400 to 1800 cm^{-1}.

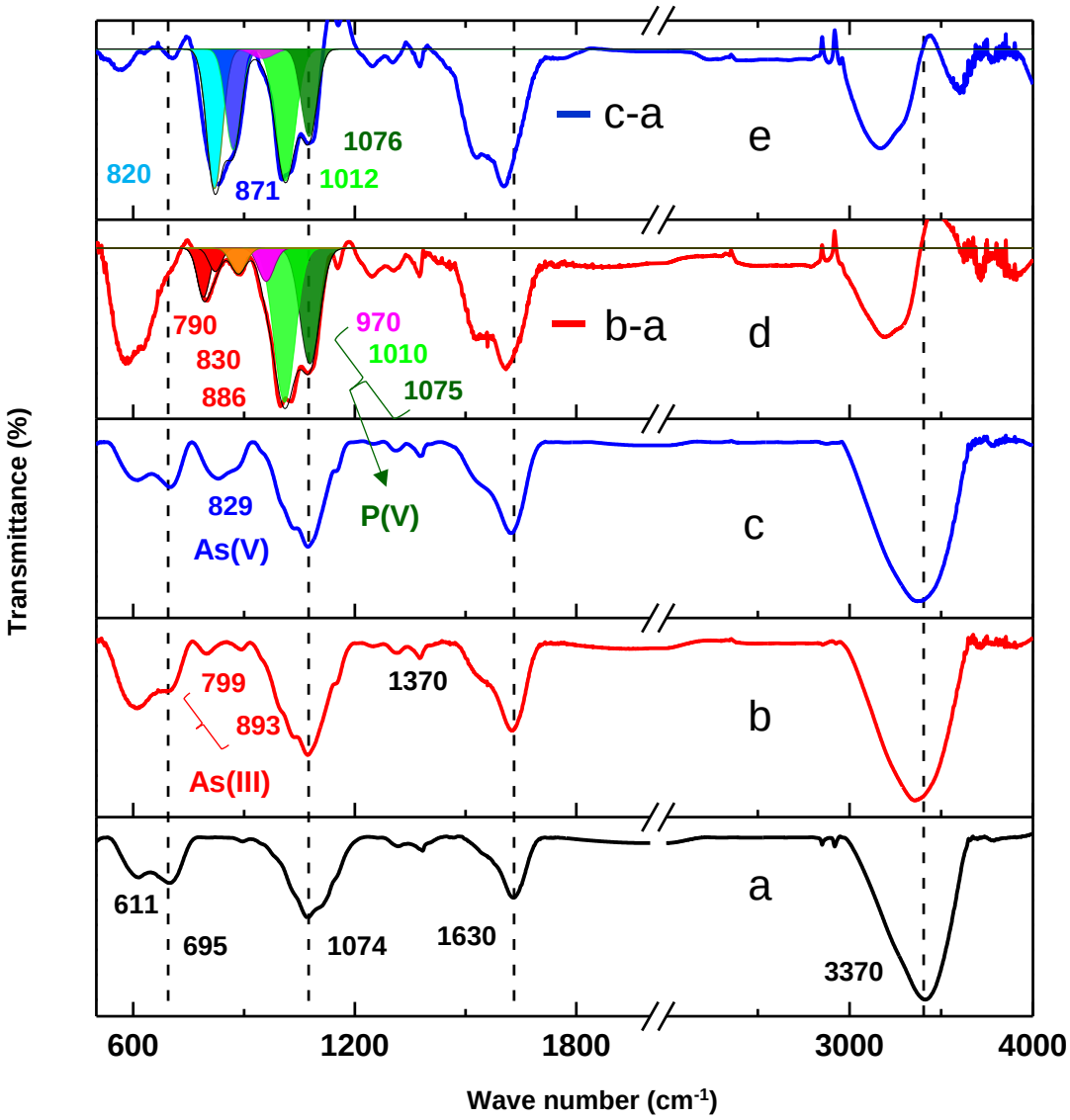

Figure S3. FTIR spectra of CM2LF (a) before adsorption, (b) AP_{mix1} and (c) AP_{mix2} adsorption. (d) Spectrum after subtraction (curve b-a). (e) Spectrum after subtraction (curve c-a).

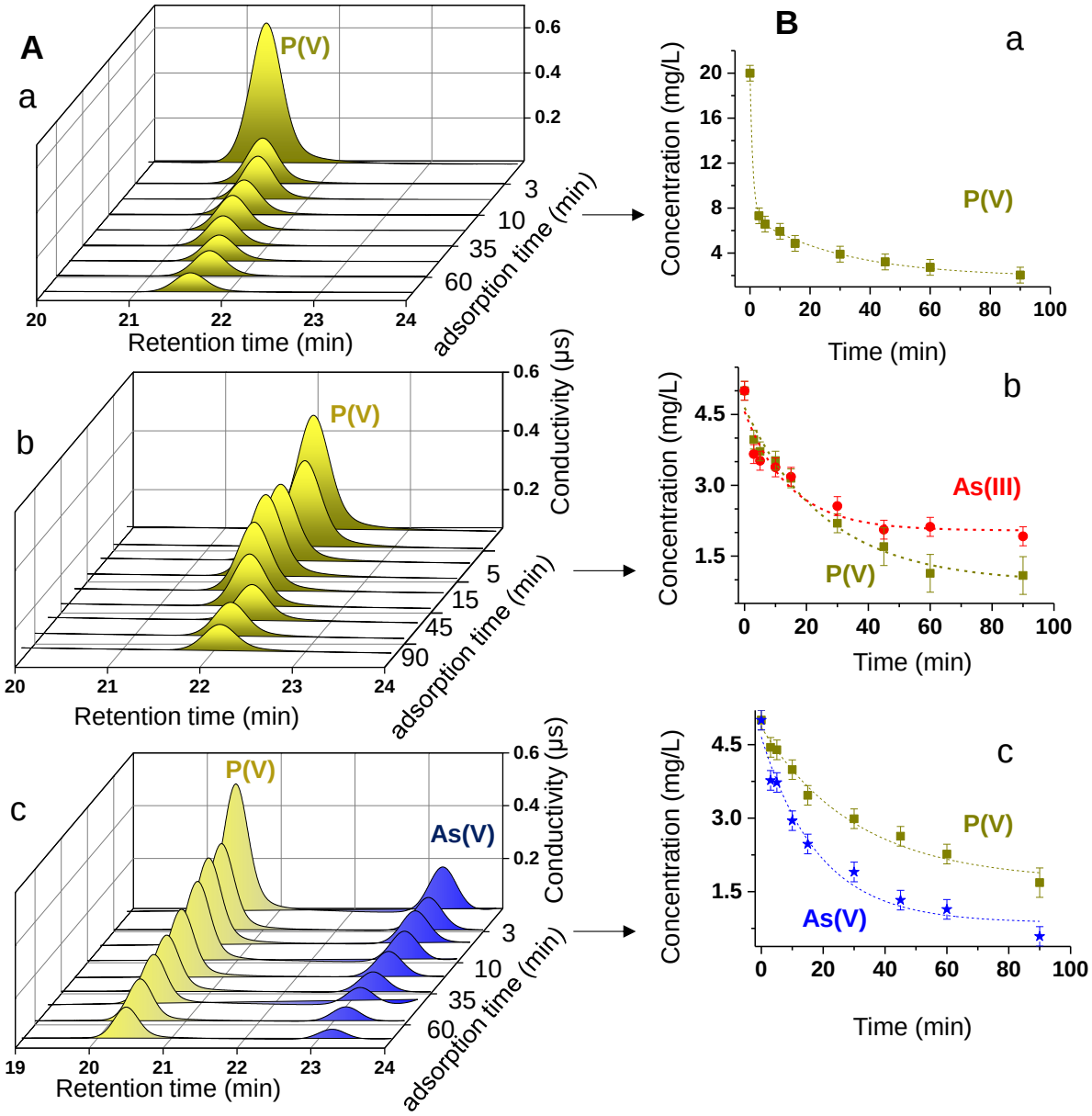

Figure S4. Time-dependent ion chromatograms showing the interaction of CM2LF with A) a) P(V), b) AP_{mix1} and c) AP_{mix2}. Their concentration versus time plots are shown in B). For As(III) analysis ICP-MS is used.

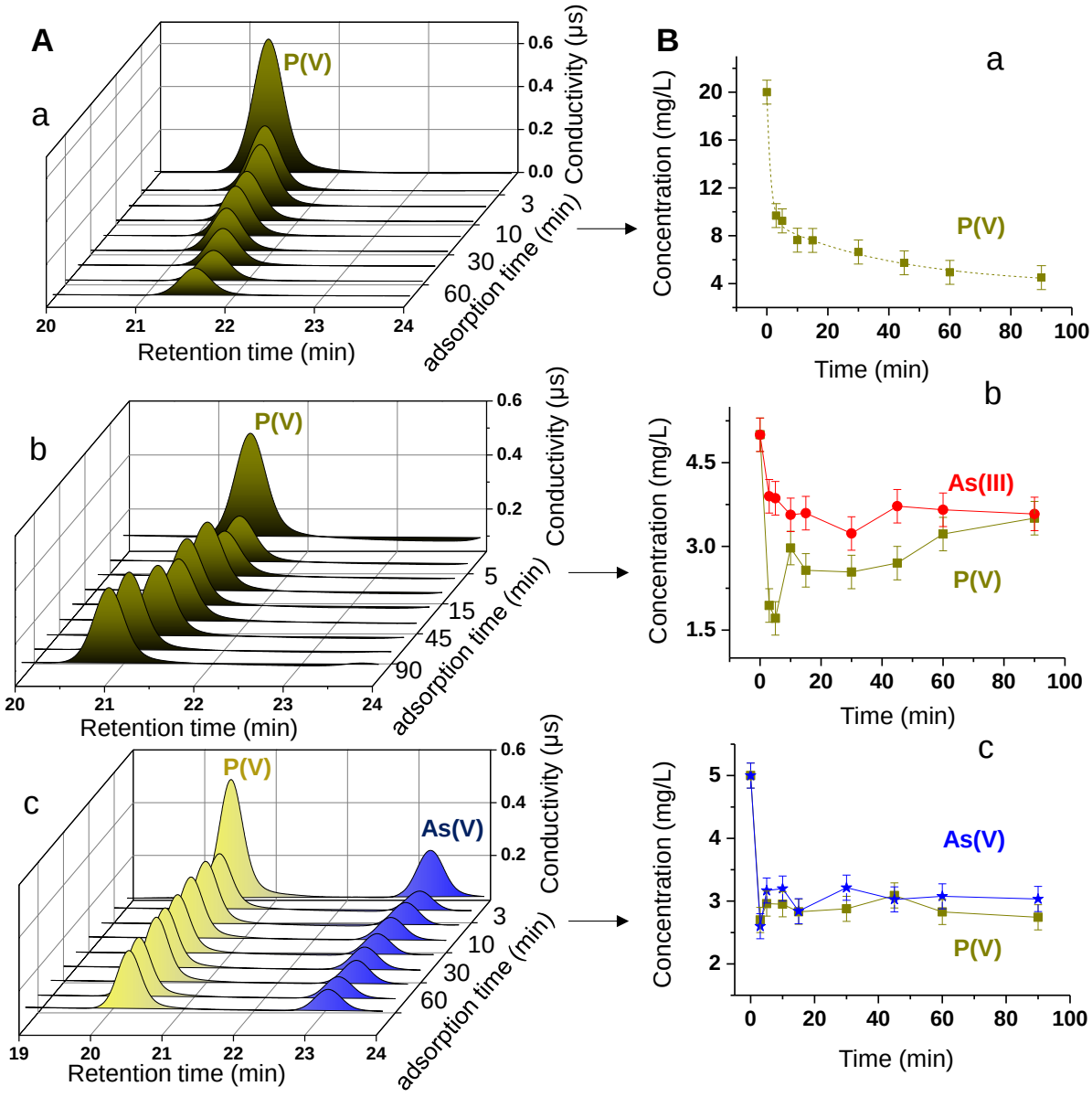

Figure S5. Time-dependent ion chromatograms showing the interaction of magnetite with A) a) P(V), b) AP_{mix1}, and c) AP_{mix2}. Their concentration versus time plots are shown in B). For As(III) analysis ICP-MS is used.

Adsorption kinetics can be expressed by using pseudo-second-order equation:

$$\frac{dq_t}{dt} = k(q_e - q_t)^2 \qquad \text{Equation (1)}$$

Where, q_t is the adsorption capacity of given material at time t, q_e is the adsorption capacity of the material at equilibrium and k is the pseudo-second-order rate constant, where initial rate is h = $kq_e{}^2$. Integration of equation (1) with limits t = 0 to t and applying boundary conditions q_t = 0 at t = 0 gives,

$$\frac{t}{q_t} = (\frac{1}{q_e})t + \frac{1}{kq_e{}^2} \qquad \text{Equation (2)}$$

The values of k and q_e can be calculated by plotting t/q_t versus t.

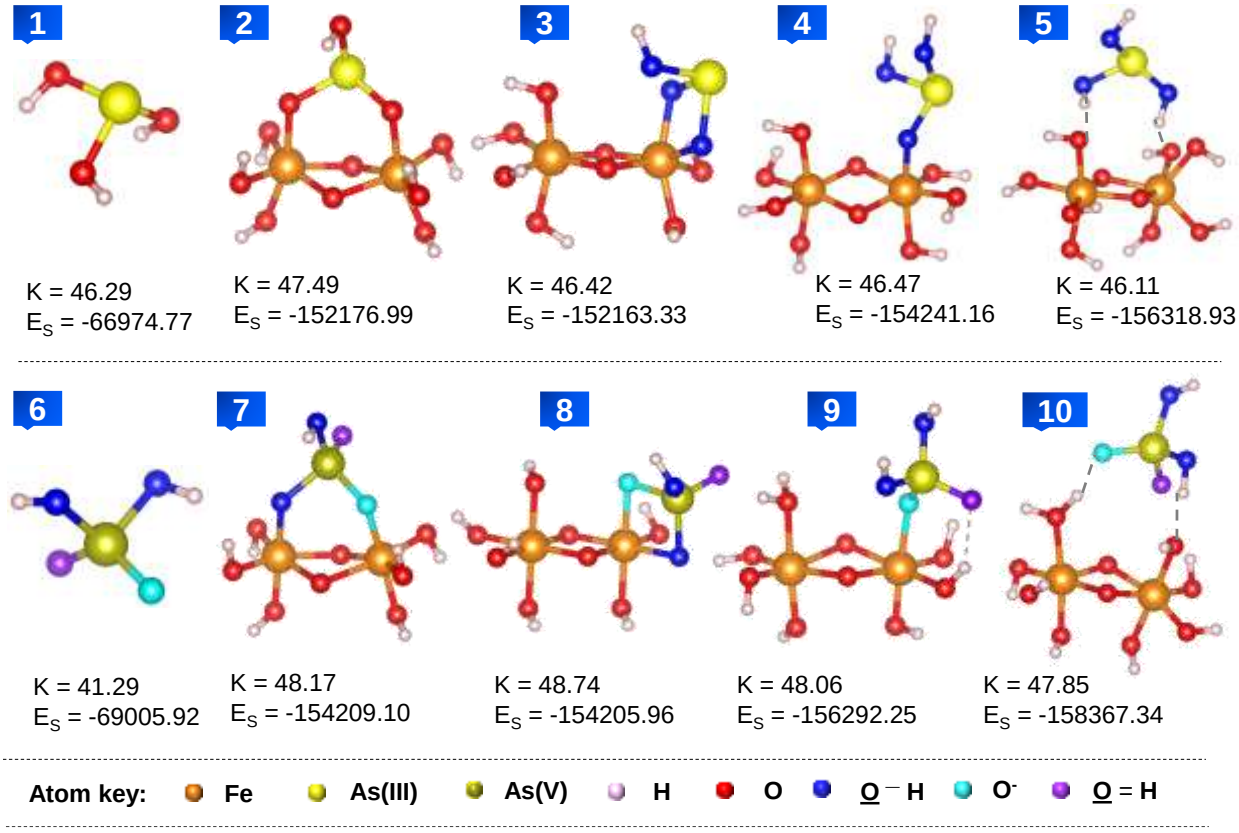

Figure S6. Theoretical binding energies (T_{BE1}) of As 3d in standard species 1) H_3AsO_3 and 6) $H_2AsO_4^{1-}$. As(III/V) species can form complex with a small ferrihydrite cluster in various ways: As(III) can bind as 2) bidentate binuclear complex (^{2}C), 3) bidentate mononuclear complex (^{2}E), 4) monodentate mononuclear complex (^{1}V) and 5) outer-sphere complex (T). Similarly, the corresponding As(V) ferrihydrite complexes are shown as 7), 8), 9) and 10). Here, theoretical binding energies (K = −E = T_{BE1}) of As 3d in arsenic complexes and their energies (E_s) are reported in eV.

Supporting Table 1

Table S1. XPS data of CM2LF and MAG before and after treated with P(V), AP_{mix1}, and AP_{mix2}.

Adsorbate	pH	Adsorbent	P 2p eV	Shift eV	As 3d eV	Shift eV	Fe $2p_{3/2}$ eV	Shift eV	Studies
		KH_2PO_4	133.4	---					current
		$NaAsO_2$			44.2				previous[6]
		$Na_2HAsO_4 \cdot 7H_2O$			44.8				previous[6]
CM2LF							Fe(III): 708.5		current
CM2lF	5	P(V)	134.2	0.8			Fe(III): 708.9	0.4	current
	9	P(V)	133.6	0.2			Fe(III): 709.1	0.6	current
	7	P(V)	134.1	0.7			Fe(III): 708.8	0.3	current
		As(III)			45.1	0.9			previous[6]
		As(III) + P(V)	134	0.5	45.4	1.2	Fe(III): 708.7	0.2	current
		As(V)			45.3	0.5			previous[6]
		As(V) + P(V)	134.4	1.0	46.5	1.7	Fe(III): 708.6	0.1	current
MAG							Main peak: 707.9 Fe(II): 706.9 Fe(III): 708.6		current
MAG	5	P(V)	134.5	1.1			Main peak: 708.5 Fe(II): 707.4 Fe(III): 709.1	0.6 0.5 0.5	current
	9	P(V)	132.8	-0.6			Main peak: 707.9 Fe(II): 706.8 Fe(III): 708.5	0.0 -0.1 -0.1	current
	7	P(V)	134.0	0.6			Main peak: 708.3 Fe(II): 707.2 Fe(III): 708.9	0.4 0.3 0.3	current
		As(III)			44.3	0.1			previous[6]
		As(III) + P(V)	133.7	0.1	45.7	1.5	Main peak: 708.5 Fe(II): 707.8 Fe(III): 709.3	0.6 0.7 0.7	current
		As(V)			45.5	0.7			previous[6]
		As(V) + P(V)	134.1	0.5	46.6	1.8	Main peak: 708.4 Fe(II):707.5 Fe(III): 709.1	0.5 0.6 0.6	current

Supporting Table 2

Table S2. DFT calculations for the P 2p binding energy of two phosphate species and each type of phosphate surface complex.

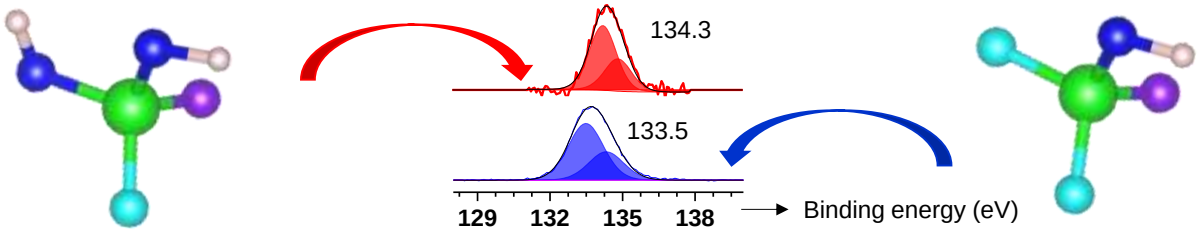

Species & Complexes	Optimized structure (A.U.)	After excitation (A.U.)	K (A.U.)	R (A.U.)	Δ (A.U.)	$\Delta = T_{BE2}$ (eV)	Method	Solvent effect
$H_2PO_4^{1-}$	-643.5993	-643.4714	4.6035	0.1279	4.7314	128.7501	B3LYP	
HPO_4^{2-}	-642.8234	-642.9396	4.3536	-0.1162	4.2374	115.3056	B3LYP	
$H_2PO_4^{1-}$	-643.7020	-643.4810	4.7808	0.2209	5.0018	136.1076	B3LYP	water
HPO_4^{2-}	-643.1887	-643.0357	4.7082	0.1530	4.8611	132.2788	B3LYP	water
$H_2PO_4^{1-}$	-641.4873	-641.3325	5.2826	0.1548	5.4374	147.9595	HF	
HPO_4^{2-}	-640.7106	-640.8178	5.0302	-0.1072	4.9230	133.9621	HF	
$H_2PO_4^{1-}$	-641.5943	-641.3859	5.4615	0.2084	5.6699	154.2869	HF	water
HPO_4^{2-}	-641.0802	-640.9102	5.3863	0.1700	5.5563	151.1968	HF	water
^2C	-3776.6787	-3776.4137	4.8545	0.2649	4.5895	124.8878	B3LYP	
^2E	-3775.6640	-3775.2396	5.0147	0.4245	4.5902	124.9057	B3LYP	
^1V	-3851.9797	-3851.6604	5.0094	0.3193	4.6901	127.6232	B3LYP	
^1V-H	-3851.8156	-3851.5166	4.8741	0.2989	4.5752	124.4970	B3LYP	
T	-3928.2736	3927.9462	4.8715	0.3274	4.5441	123.6504	B3LYP	
^1T-H	-3928.1196	3928.7922	4.6995	0.3274	4.3721	118.9698	B3LYP	

* Complexes: ^{2}C = bidentate binuclear, ^{2}E = bidentate mononuclear, ^{1}V = monodentate mononuclear, ^{1}V-H = deprotonated monodentate mononuclear, T = outer-sphere, and T = deprotonated outer-sphere.

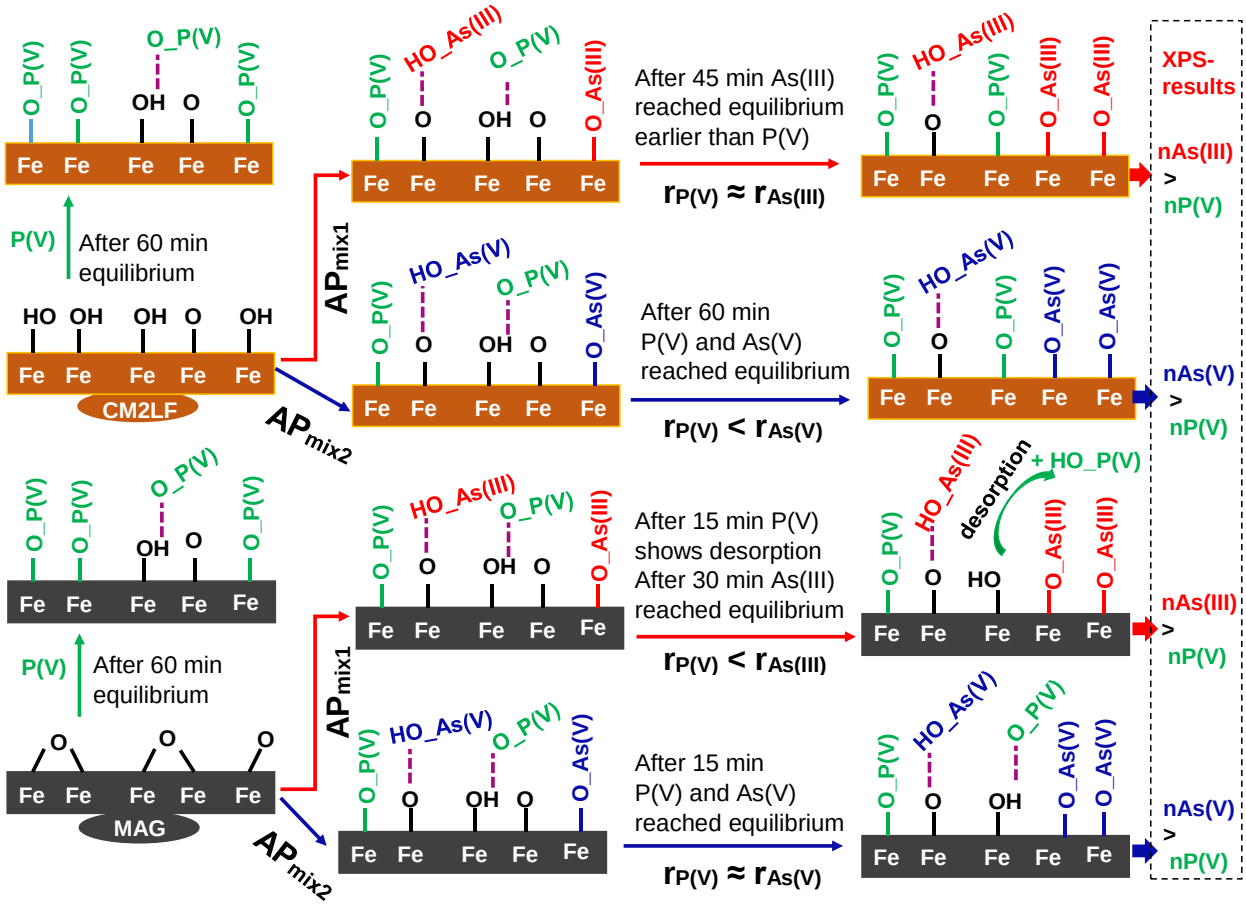

Figure S7. Schematic illustration of P(V) interference in the As(III/V) adsorption based on time dependent ion chromatography and XPS studies. The term r_x means rate of ions adsorption (X= P(V)/As(III)/As(V)). nAs(III/V) means no of adsorbed arsenic species, nP(V) no of adsorbed phosphate species.

Table S3. Interference of P(V) on the As(III/V) adsorption (experimental results).

Adsorbent	Species pH 7	Type of experiment	P 2p (eV)	Shift	As 3d (eV)	Shift	Electrostatic effects on P 2p/As 3d levels	Adsorption kinetics (PSO)
CM2LF	$H_xPO_4^{y-}$	Reference for P(V)	134.1					Solely follows PSO
	H_3AsO_3	Reference for As(III)			45.1			Solely follows PSO
	$H_xPO_4^{y-}$ + H_3AsO_3	AP_{mix1}	134.0	no	45.4	blue	no effect on P 2p effect on As 3d	P(V) and As(III) partially follows PSO
	$H_xAsO_4^{y-}$	Reference for As(V)			45.3			Solely follows PSO
	$H_xPO_4^{y-}$ + $H_xAsO_4^{y-}$	AP_{mix2}	134.4	blue	46.5	blue	effect on P 2p effect on As 3d	P(V) and As(V) partially follows PSO
MAG	$H_xPO_4^{y-}$	Reference for P(V)	134.1					Solely follows PSO
	H_3AsO_3	Reference for As(III)			44.3			Solely follows PSO
	$H_xPO_4^{y-}$ + H_3AsO_3	AP_{mix1}	133. 7	red	45.7	blue	effect on P 2p effect on As 3d	P(V) shows desorption As(III) equilibrium shifted
	$H_xAsO_4^{y-}$	Reference for As(V)			45.5			
	$H_xPO_4^{y-}$ + $H_xAsO_4^{y-}$	AP_{mix2}	134. 1	no	46.6	blue	no effect on P 2p effect on As 3d	P(V) and As(V) reached early equilibrium

***** PSO: pseudo-second-order

As 3d peak got blue-shifted for As(III) in case of AP_{mix1} as compared to only As(III) adsorbed materials (Table S3 and Figure 5). Similar results were observed in the case of AP_{mix2}. These

results suggest that the speciation of adsorbed As(III) (ratio of chemisorbed and physisorbed species) on CM2LF and MAG gets affected due to the presence of P(V). We can conclude that P(V) ions are affecting the As(III/V) speciation on CM2LF and MAG. As far as adsorption kinetics is concerned, As(III/V) ions follow pseudo-second-order kinetics when alone and follow pseudo-second-order kinetics partially in presence of P(V) in case of AP_{mix1} and AP_{mix2} adsoprtion. Thus kinetics and adsorption equilibrium for As(III/V) get affected by presence of P(V) ions (Figure S7).

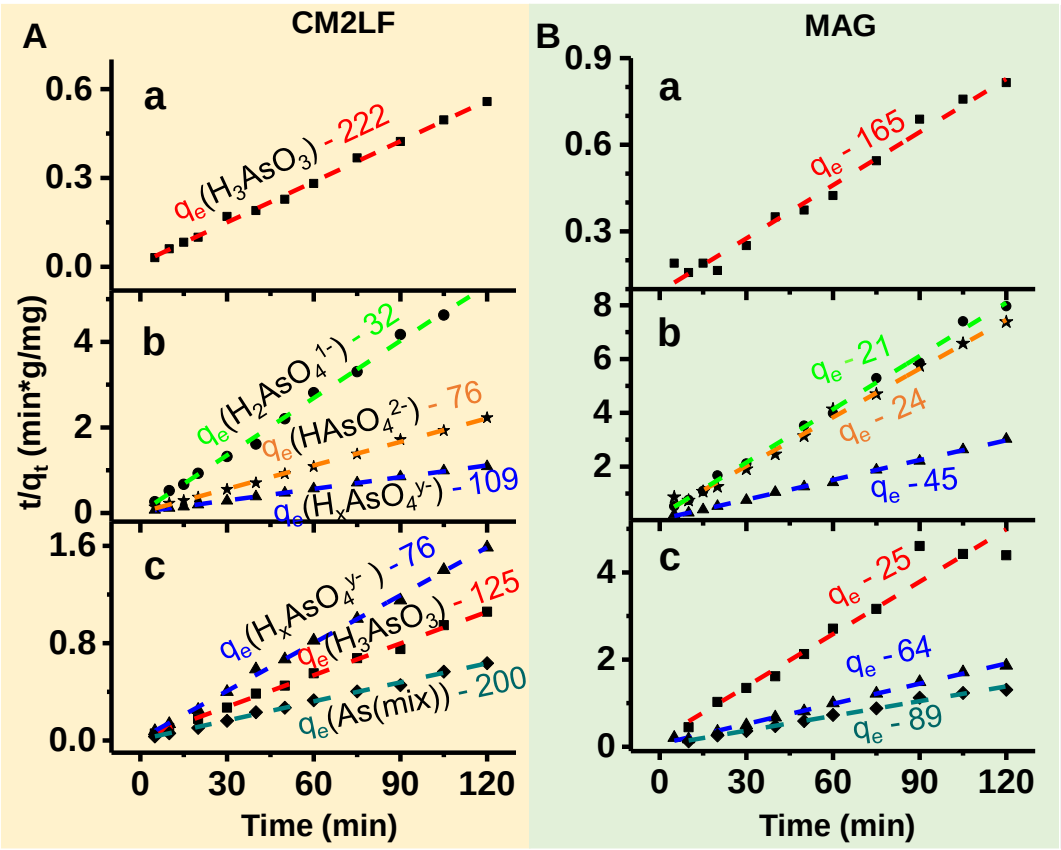

Figure S8. Pseudo-second-order kinetics for A) CM2LF and B) MAG, where a, b and c represent As(III), As(V) and As(mix) removal, respectively. The unit of q_e and q_t is mg/g. Kinetics data taken from Sudhakar et al., 2017[6].

Sustainability aspects of CM2LF and magnetite materials

CM2LF has a composite structure where the metastable 2-line ferrihydrite phase ($Fe_2O_3.0.5H_2O$) is confined in biopolymeric cages of chitosan. Particles used here are of 72 μm in size.[1] It is synthesized by the hydrolysis of a metal precursor (Fe^{3+})–chitosan complex using an alkaline medium followed by washing and drying it at ambient conditions. On the other hand, commercial grade magnetite nanoparticles used in this work are iron oxide (Fe_3O_4) grains of about 40 nm size that exhibit superparamagnetic properties at ambient temperature and can be prepared by various methods. Some reports follow refluxing of FeOOH and oleic acid in 1-octadecene[7], while others have reported alkali precipitation of solution with a molar ratio of Fe(II)/Fe(III) = 0.5 in deoxygenated water resulting in a black precipitate.[8]

1. Material efficiency: The removal effiency of a material can be considered based on its selectivity and uptake capacity for the contaminant. Results from the present study confirm that CM2LF performed better than magnetite (MAG) for As(III/V) uptake in presence of P(V) and shows higher affinity for As(III) and As(V) species than P(V) at neutral pH. On the other hand, our previous study has shown that the maximum adsorption capacity of CM2LF determined by Langmuir isotherm is 100 mg/g for AsIII/AsV and it has been tested in real time conditions[1]. For magnetite, it is 40 mg/g determined through time-dependent aqueous Raman measurements, but using Langmuir isotherm, it is 12.7 mg/g[9], while activated alumina shows a capacity of 15.9 mg/g[1]. Loading or dosage required is lower for materials exhibiting higher uptake capacity, leading to lesser waste generation and thus serves as a more sustainable option for purification processes.
2. Material stability: Although nanomaterials have been widely studied for their application in water purification, it is known that using loose nanoparticles for the same purpose may lead nanoparticle aggregation, conversion or dissolution/leaching, leading to secondary water pollution. These factors have led to the importance of using nanocomposites like CM2LF where nanoparticles are trapped inside templates making the system robust and stable, thus providing a more beneficial option. For example, there are reports where oxidation of magnetite takes place in aerated aqueous media[10] to form more stable iron oxide form (hematite: α-Fe_2O_3) or dissolution of magnetite by thermal or microbial reduction.[11-12] proving

that it is a less stable option to use for water purification. While, CM2LF has been tested for metals (Fe, As) and carbon leaching into water after its use in purification cartridges for long time by TCLP (Toxicity Characteristic Leaching Protocol) and TOC (Total Organic Carbon) procedures, it has shown negligible leaching, confirming its mechanical stability and thus making it more environment friendly.

3. Cost of production: Affordability is another factor to determine sustainability of materials. While, commercial magnetite (Fe II/III oxide, 97%, Alfa Aesar) costs \$51/kg[13] and has come down from an initial cost of production like \$2600/kg[7], bulk scale CM2LF is less than \$15/kg and the process requires no electrical power and no organic solvents. Hence, CM2LF can sustainably cater to larger strata of people, including economically weaker sections.

REFERENCES

1. Kumar, A. A.; Som, A.; Longo, P.; Sudhakar, C.; Bhuin, R. G.; Gupta, S. S.; Anshup; Sankar, M. U.; Chaudhary, A.; Kumar, R.. et al., Confined Metastable 2-Line Ferrihydrite for Affordable Point-of-Use Arsenic-Free Drinking Water. *Advanced Materials* **2017**, *29*, 1604260.
2. Mastronarde, D. N., Serialem. A Program for Automated Tilt Series Acquisition on Tecnai Microscopes Using Prediction of Specimen Position. *Microscopy and Microanalysis* **2003**, *9*, 1182.
3. Nonappa, N. E., Peter. Electron Tomography of Whole Mounts. *In: Imaging & Microscopy.* **2019**, *21*.
4. Kremer, J. R.; Mastronarde, D. N.; McIntosh, J. R. Computer Visualization of Three-Dimensional Image Data Using Imod. *Journal of Structural Biology* **1996**, *116*, 71-76.
5. Engelhardt, P. In Electron Microscopy: Methods and Protocols, Ed. J. Kuo, Humana Press, Totowa, Nj, **2007**.
6. Sudhakar, C.; Anil Kumar, A.; Bhuin, R. G.; Sen Gupta, S.; Natarajan, G.; Pradeep, T. Species-Specific Uptake of Arsenic on Confined Metastable 2-Line Ferrihydrite: A Combined Raman-X-Ray Photoelectron Spectroscopy Investigation of the Adsorption Mechanism. *ACS Sustainable Chemistry & Engineering* **2018**, *6*, 9990-10000.
7. Yavuz, C. T.; Mayo, J. T.; Carmen, Suchecki; Jennifer, Wang; Adam, Z. Ellsworth; Helen, D'Couto; Elizabeth, Quevedo; Laura, Gonzalez; Christina, Nguyen; Vicki, L. Colvin. Pollution Magnet: Nano-Magnetite for Arsenic Removal from Drinking Water. *Environmental Geochemistry and Health* **2010**, *32*, 327-334.
8. Kang, Y. S.; Risbud, S.; Rabolt, J. F.; Stroeve, P. Synthesis and Characterization of Nanometer-Size Fe3o4 and Γ-Fe2o3 Particles. *Chemistry of Materials* **1996**, *8*, 2209-2211.
9. Shahid, M. K.; Phearom, S.; Choi, Y.-G. Adsorption of Arsenic (V) on Magnetite-Enriched Particles Separated from the Mill Scale. *Environmental Earth Sciences* **2019**, *78*, 65.

10. Taylor, P., and Owen, D G. Oxidation of Magnetite in Aerated Aqueous Media. Technical Report: Canada, **1993**.
11. Dinov, K.; Ishigure, K.; Matsuura, C.; Hiroishi, D. Solubility of Magnetite in High Temperature Water and an Approach to Generalized Solubility Computations. *Journal of Nuclear Materials* **1993**, *207*, 266-273.
12. Kostka, J. E.; Nealson, K. H. Dissolution and Reduction of Magnetite by Bacteria. *Environmental Science & Technology* **1995**, *29*, 2535-2540.
13. Alfa Aesar, https://www.Fishersci.Com/Shop/Products/Iron-Ii-Iii-Oxide-97-Metals-Basis-Alfa-Aesar-3/Aa12374a1 (accessed Mar16, 2021).